Nanoscale

Accepted Manuscript

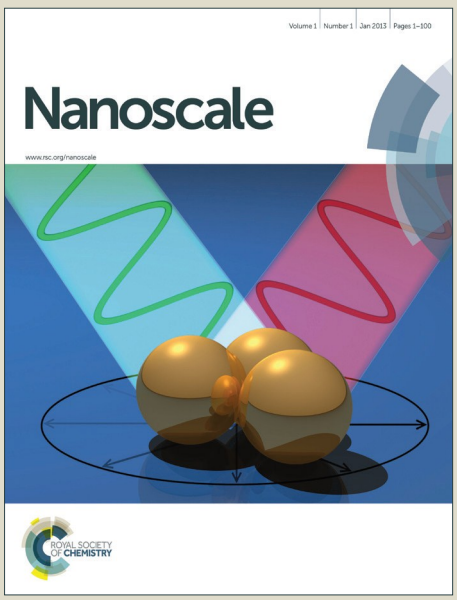

ROYAL SOCIETY OF CHEMISTRY

www.rsc.org/nanoscale

Journal Name

RSCPublishing

COMMUNICATION

Metal-Insulator Crossover in Multilayer MoS_2

Min Ji Park, [a] Sum-Gyun Yi, [a] Joo Hyung Kim [a] and Kyung-Hwa Yoo [a*]

Cite this: DOI: 10.1039/xoxxoooooox

Received ooth January 2012,
Accepted ooth January 2012

DOI: 10.1039/xoxxoooooox

www.rsc.org/

The temperature dependence of electrical transport properties was investigated for multilayer MoS_2 field effect transistor devices with thicknesses of 3 ~ 22 nm. Some devices showed typical n-type semiconducting behavior, while others exhibited the metal-insulator crossover (MIC) from metallic to insulating conduction at finite temperatures. The latter effect occurred near zero gate voltage or at high positive gate voltages. Analysis of Raman spectroscopy revealed the key difference that devices with the MIC had a metallic 1T phase as well as a semiconducting 2H phase, whereas devices without the MIC did not have a metallic 1T phase. These results suggest that the metallic 1T phase may contribute to inducing the MIC.

Molybdenum disulphide (MoS_2) is a layered transition-metal dichalcogenide crystal consisting of a vertical stack of atomic layers bound by van der Waals forces. Each layer is constructed from S-Mo-S′ triple atomic planes with strong in-plane bonding. Single-layer MoS_2 appears in two distinct symmetries with different electronic structures: the semiconducting 2H, where each Mo has a trigonal prismatic coordination with the nearby S atoms, and metallic 1T phases, where each Mo octahedrally coordinates with the nearby S atoms.[1-7] The most stable polytype of bulk MoS_2 is the 2H phase. Mechanical exfoliation of bulk 2H MoS_2 leads to the formation of single layer MoS_2 in the 2H phase.[1-4] In contrast, chemically exfoliated MoS_2 single layers are in the 1T phase since the Li intercalation stabilizes a 1T Li_xMoS_2 polytype.[8-10] However, the 1T phase is metastable, so mild annealing leads to a gradual transformation to the 2H phase.[11]

Single- or multi-layer MoS_2 prepared by mechanical exfoliation has been extensively studied for its unique electrical, optical, and mechanical properties.[12-24] Multi-layer MoS_2 is a semiconductor with an indirect bandgap of ~1.2 eV, while single-layer MoS_2 presents a direct bandgap of 1.8 eV due to quantum confinement.[16-17, 25-26] The mechanical strength of MoS_2 is about 30 times greater than that of steel due to its strong in-plane bonding.[22-23] To gain a fundamental understanding of its electronic properties, temperature dependence measurements of the electrical transport properties are required. Previous low-temperature measurements in monolayer MoS_2 have shown that the mobility (μ) is limited by phonon scattering at high temperatures; thus, μ follows a $\mu \sim T^{-\gamma}$ temperature dependence with the exponent $\gamma \approx 0.6 \sim 1.7$.[26-28] Furthermore, the metal-insulator transition (MIT) has been observed at a conductivity (σ) of approximately e^2/h in highly doped monolayer MoS_2, where e is the electron charge and h is the Planck's constant.[26-30] In contrast, there are few reports that have measured the temperature dependence of the electrical transport properties for multilayer MoS_2. To determine whether multilayer MoS_2 exhibits a similar behavior to monolayer MoS_2, we investigated the temperature dependence of the electrical transport properties for more than 20 multilayer MoS_2 field effect transistor (FET) devices. We identified three representative characteristics. Some devices showed typical n-type semiconducting behaviors at all temperatures, while the other devices exhibited the MIC at finite temperatures. However, unlike highly doped monolayer MoS_2,[26, 27] our devices were made of multilayer MoS_2 and crossover from metallic to insulating conduction was found at a finite temperature, leading to a peak of σ. These results suggested that its origin might be different from the origin of the MIT observed in monolayer MoS_2.

To explore the origin of the MIC in multilayer MoS_2, we measured the Raman spectra as they are a useful tool for studying the metallic 1T and semiconducting 2H phases.[5-10,31-32] Other than the typical E^1_{2g} and A_{1g} modes, additional Raman peaks were observed for devices with the MIC, but not for devices without the MIC. Since the additional Raman peaks are probably due to the 1T phase,[9,31] these observations suggest that the metallic 1T phase may coexist with the semiconducting 2H phase in multilayer MoS_2, and that this metallic 1T phase may contribute to inducing the MIC.

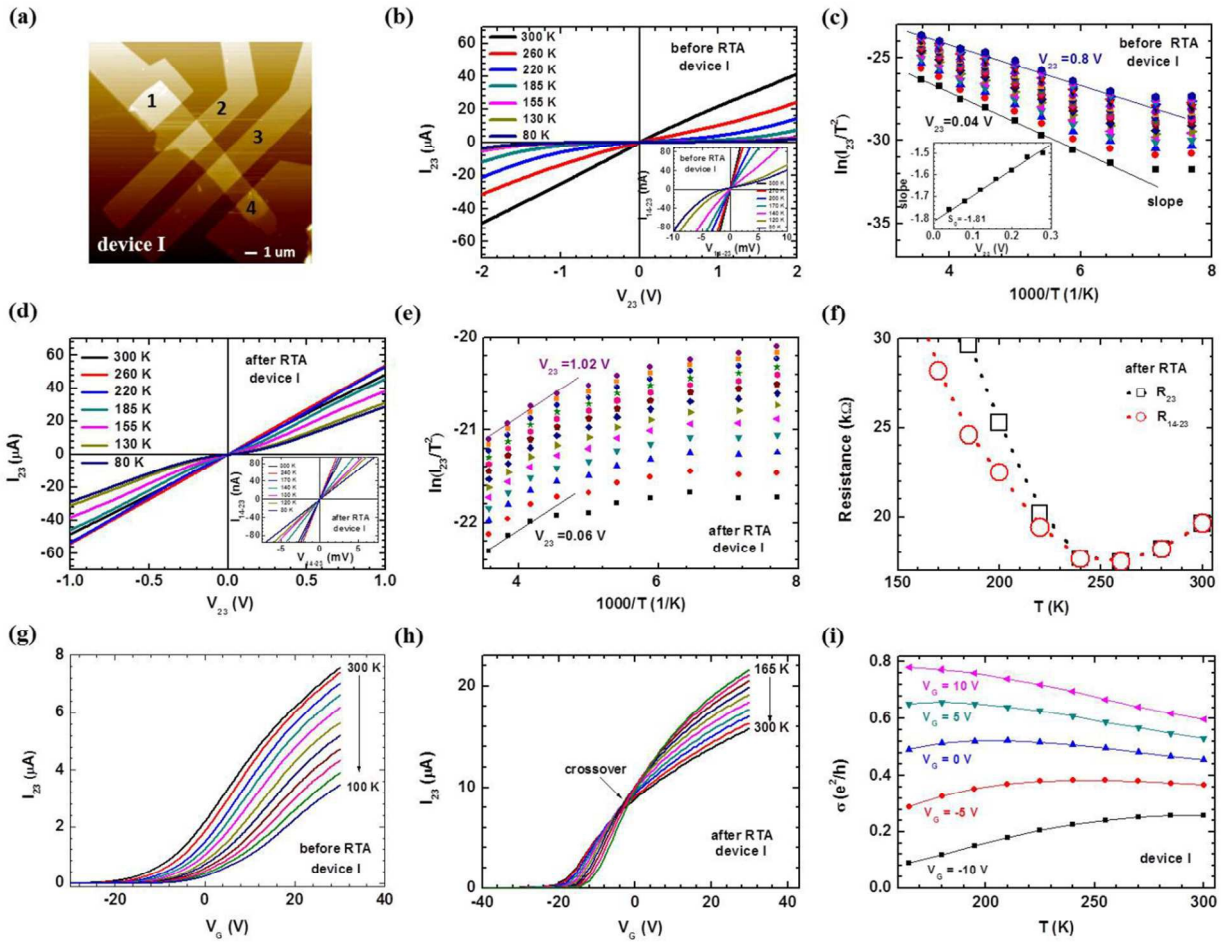

Figure 1. **(a)** AFM image of the multilayer MoS_2 based field-effect device (device I) contacted by four electrodes. **(b)** Temperature dependence of I_{23}-V_{23} curves measured using electrodes 2 and 3 for device I before RTA. The inset shows temperature dependence of $I_{14\text{-}23} - V_{14\text{-}23}$ curves measured by passing a current through electrodes 1 and 4 and measuring a voltage through electrodes 2 and 3 for device I before RTA. **(c)** $\ln(I_{23}/T^2)$ versus $1000/T$ at different values of V_{23} for device I before RTA. The inset shows the slope estimated from $\ln(I/T^2)$ versus $1000/T$ as a function of V_{23}. ***(d)*** Temperature dependence of I_{23}-V_{23} curves measured using electrodes 2 and 3 for device I after RTA. The inset shows temperature dependence of $I_{14\text{-}23} - V_{14\text{-}23}$ curves measured by passing a current through electrodes 1 and 4 and measuring a voltage through electrodes 2 and 3 for device I after RTA. **(e)** $\ln(I_{23}/T^2)$ versus $1000/T$ at different values of V_{23} for device I after RTA. **(f)** Temperature dependence of R_{23} and $R_{14\text{-}23}$ estimated for device I before and after RTA. I_{23}-V_G transfer curves measured at different temperatures for device I **(g)** before and **(h)** after RTA. **(i)** Temperature dependence of σ for different values of V_G in device I after RTA.

First, we fabricated a multilayer MoS_2 FET device with four electrodes (Figure 1(a), device I) using a typical mechanical exfoliation method. Briefly, MoS_2 flakes were transferred from MoS_2 crystals to Si substrates with thermally grown SiO_2 (300 nm), and then Au (50 nm)/Cr (5 nm) electrodes were patterned using electron-beam lithography and lift-off techniques. The thickness of the transferred MoS_2 flake measured by an atomic force microscope was about 9.8 nm. Figure 1(b) shows the current (I) – voltage (V) curves measured using electrodes 2 and 3 (I_{23}-V_{23}). The inset of Figure 1(b) presents the results from passing a current through electrodes 1 and 4 and measuring the voltage through electrodes 2 and 3 ($I_{14\text{-}23}$ - $V_{14\text{-}23}$) at various temperatures. Both I - V curves were linear at 300 K. The room temperature resistance was estimated to be $R_{4\text{-probe}} \approx 29.3$ kΩ from the $I_{14\text{-}23}$-$V_{14\text{-}23}$ curve and $R_{23} \approx 37.4$ kΩ from the I_{23}-V_{23} curve; therefore, the contact resistance (R_C) was calculated to be about 4.1 kΩ from the relationship $R_C = (R_{23} - R_{4\text{-probe}})/2$. The contact resistance R_C is mainly ascribed to the Schottky barrier at the MoS_2-metal contact. According to a thermionic emission model, the electrical transport across a Schottky contact into a material is described by[33-35]

$$I \approx AA^*T^2 \exp\left[-\frac{e}{k_BT}\left(\Phi_B - \frac{V}{n}\right)\right] \qquad (1)$$

where A is the contact area of the junction, A^* is the effective Richardson constant, e is the electron charge, Φ_B is the Schottky barrier height, n is the ideality factor, and V is the drain-source bias voltage. To extract Φ_B, $\ln(I_{23}/T^2)$ was plotted as a function of $1000/T$ for various values of V_{23} (Figure 1(c)). Negative slopes were found and the slope increased linearly with V_{23}. From the intercept (S_0), Φ_B was estimtaed to be approximately156 meV (inset of Figure 1(c)).

To decrease R_C or Φ_B, rapid thermal annealing (RTA) was performed at 200°C for 3 min in an N_2 atmosphere. The I_{23} - V_{23} and $I_{14\text{-}23}$ -$V_{14\text{-}23}$ curves measured at various temperatures after RTA are shown in Figure 1(d) and its inset, respectively. After RTA, R_{23} and $R_{14\text{-}23}$ decreased to about 19.65 and 19.63 kΩ at 300 K, respectively, resulting in $R_C \approx 0.02$ kΩ. Figure 1(e)

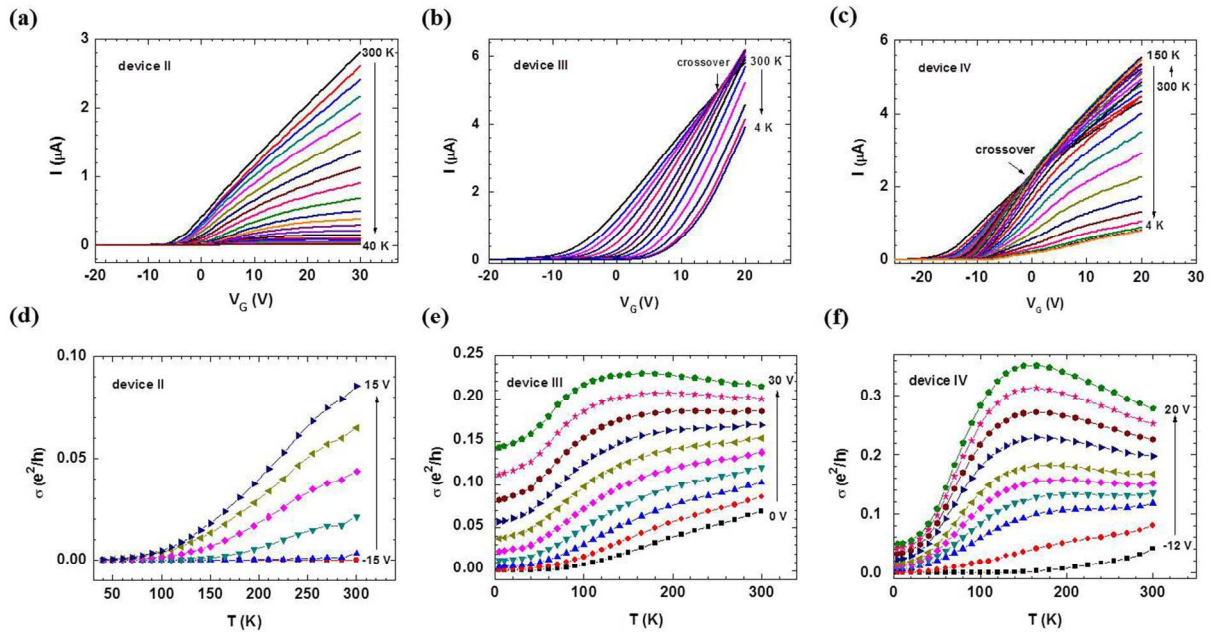

Figure 2. I-V_G transfer curves measured at different temperatures for devices II **(a)**, III **(b)**, and IV **(c)**, where I was measured using two electrodes. Temperature dependence of σ for different values of V_G in devices II **(d)**, III **(e)**, and IV **(f)**.

depicts the plot of $\ln(I_{23}/T^2)$ versus $1000/T$ after RTA. Unlike the data obtained before RTA, positive slopes were found at various V_{23}, supporting that Φ_B was reduced to near zero by RTA, leading to $R_C \approx 0$. The temperature dependence of R_{23} and $R_{14\text{-}23}$ measured after RTA is shown in Figure 1(f). For $T > 240$ K, R_{23} was nearly same as $R_{14\text{-}23}$, indicating that R_C was nearly negligible above 240 K. Furthermore, as the temperature decreased, R_{23} and $R_{14\text{-}23}$ decreased until a temperature of about 240 K, and then they increased at lower temperatures, suggesting that the MIC occurred around 240 K.

The current (I_{23}) – gate voltage (V_G) transfer curves of device I measured at various temperatures before and after RTA are shown in Figures 1(g) and (h), respectively. Before RTA, device I showed a typical n-type semiconducting behavior. However, the annealed device exhibited a crossover near $V_G \approx 0$ V although the crossover temperature was dependent on V_G. For positive V_G, the conductivity ($\sigma = \frac{I}{V} \cdot \frac{L}{W}$) increased with decreasing temperature, indicating metallic behavior, whereas σ decreased with decreasing temperature for negative V_G (Figure 1(i)). A similar crossover was reported for the highly doped monolayer MoS_2, in which the crossover occurred at the channel conductivity on the order of e^2/h as a consequence of a two-dimensional (2D) electron gas.[36-38] However, device I exhibited crossover at $\sigma < e^2/h$ (Figure 1(i)), and it might not be regarded as a 2D electron gas since its thickness was about 9.8 nm. Therefore, the origin of the crossover observed in device I might not be related to the 2D electron gas.

To determine whether the MIC is observable in other multilayer MoS_2 FET devices besides device I, we measured the I-V_G transfer curves at various temperatures for more than 20 devices, with thicknesses ranging from 3 to 22 nm. Three representative characteristics were found, as shown in Figures 2(a), (b), and (c). The first characteristic was an absence of crossover (device II, Figure 2(a)), and the second was the presence of crossover at large positive values of V_G (device III, Figure 2(b)). Similar weak metal-like behavior has also been reported in trilayer MoS_2.[39] The last characteristic exhibited crossover around $V_G \approx 0$ V, as for device I (device IV, Figure 2(c)). Interestingly, the thickness of device IV was similar to that of device II (Table I), implying that the crossover might be observable independently of the MoS_2 layer thickness. The I-V curves measured at V_G=0 for various temperatures are shown in Figures S1 (a), (b), and (c) for devices II, III, and IV, respectively. Φ_B was estimated to be 90.1, 45.6, and 0 meV for devices II, III, and IV, respectively (Figures S1(d) - (h)). As for the annealed device I, device IV yielded $\Phi_B \approx 0$ meV,

Table I. Summary of Schottky barrier height (Φ_B), field-effect mobility (μ), and carrier concentration (n) estimated for various devices before and after RTA. ([a] μ and n were estimated at $T = 300$ K, $V_G = 20$ V)

device	thickness (nm)	before RTA			after RTA		
		Φ_B (meV)	μ [a] ($cm^2V^{-1}S^{-1}$)	n [a] (10^{12} cm^{-2})	Φ_B (meV)	μ [a] ($cm^2V^{-1}S^{-1}$)	n [a] (10^{12} cm^{-2})
I	9.8	156	31.06	4.40	0	74.41	4.43
II	22	90.1	11.11	2.87	-	-	-
III	10	45.6	25.67	3.61	-	-	-
IV	21	0	26.58	3.78	-	-	-
V	12	-	-	-	0	7.0	4.48
VI	2.7	46.1	11.21	3.50	33.67	19.88	2.96
VII	12	46	55.69	4.53	32.77	73.18	4.41
VIII	16	39.3	7.88	4.40	20	6.96	4.53

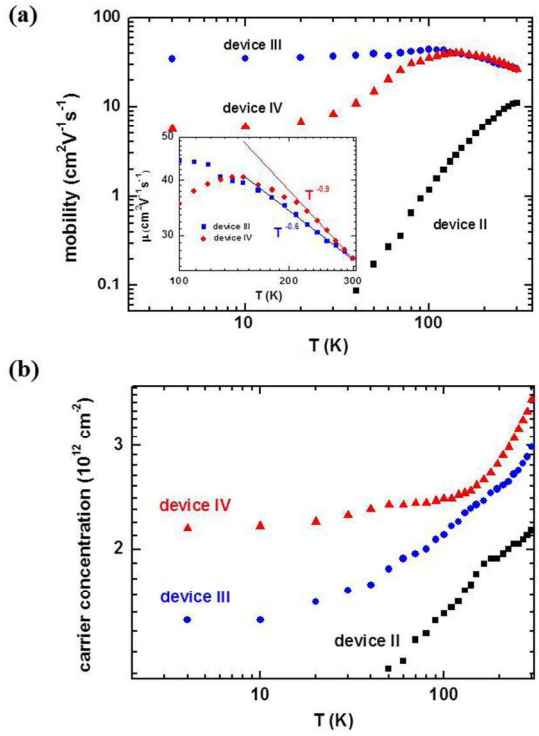

Figure 3. (a) Temperature dependence of field-effect mobility (μ) for devices II, III, and IV. The inset shows the plot of log(μ) versus log(T). **(b)** Temperature dependence of carrier concentration (n) for devices II, III, and IV.

suggesting that the low values of Φ_B may be necessary to observe the crossover.

To investigate the effect of Φ_B on I-V_G transfer curves further, we also measured the I-V_G transfer curves at different temperatures for the annealed device V, which had asymmetric I-V curves (Figure S2(a)). Different behaviors were found for positive and negative bias voltages: the presence of crossover around V_G=10 V for a positive bias voltage (Figures S2(b)), and an absence of crossover for negative bias voltages (Figures S2(c)). From the temperature dependence of the I-V curves and Eq. (1), Φ_B was estimated to be approximately 0 and 31.85 meV for positive and negative voltages, respectively (Figures S2(d) - (f)). These results supported that to observe the MIC, the contact between MoS_2 and the electrodes should be good, or that R_C became negligible due to the metallic state above the crossover temperature. The Schottky barrier Φ_B of devices I and IV might not be negligible for $V_G < 0$ V, although it was nearly zero for $V_G \geq 0$ V, as summarized in Table I. However, the crossover was observed at $V_G \approx 0$ V for both devices, so the influence of Schottky barrier on the crossover might be negligible. In fact, we also measured the I-V_G transfer curves of the annealed device I using four electrodes, and found very similar transfer curves, suggesting that the conductivity was not affected much by the contact resistance for $V_G < 0$ V.

In Figures S3(a) – (f), the I-V_G transfer curves measured at different temperatures for devices VI, VII, and VIII before and after RTA are shown. The thickness of devices VI, VII, and VIII was about 2.3, 12, and 16 nm, respectively. Before RTA, the crossover was not found for these devices, which was ascribed to the high values of Φ_B (Table I). After RTA, however, Φ_B was lowered (Table I) and the crossover appeared at positive values of V_G. Devices VI and VII with similar values of Φ_B exhibited the crossover at similar values of V_G, while device VIII with the smaller value of Φ_B showed it at the smaller value of V_G. These observations indicated that the crossover might be more closely related to Φ_B rather than the thickness of MoS_2.

The field-effect mobility (μ), estimated using the equation $\mu=(dI/dV_G)\times L/(WC_{ox}V)$,[40] is plotted as a function of temperature in Figure 3(a) for devices II, III, and IV, where L and W are the channel length and width, respectively, and $C_{OX} = \varepsilon_{OX}/d_{OX} \approx 1.21\times10^{-8}$ F (d_{OX}=300 nm is the thickness of the gate oxide and $\varepsilon_{OX} = 3\times10^{-11}$ is the dielectric constant for SiO_2). For device II, μ decreased with decreasing temperature. This was attributed to scattering from extrinsic scattering sources, including Coulomb impurity scattering and surface roughness scattering.[36-38] The μ of device III or device IV was higher than that of device II. Moreover, the μ of device III was nearly constant at low temperatures, and that of device IV decreased slowly with decreasing temperature. The latter was attributed to suppressed scattering from extrinsic scattering sources in these devices. At high temperatures, the μ of device III or device IV decreased with increasing temperature, and it followed the relationship $\mu \sim T^{-\gamma}$ at high temperatures due to phonon scattering. The exponent γ was estimated to be about 0.6 and 1.0 for devices III and IV, respectively (inset of Figure 3(a)). These values were comparable to or smaller than $\gamma \approx 0.6 \sim 1.7$, as reported for monolayer MoS_2.[26, 27]

Figure 3(b) shows the carrier concentration calculated using $n=C_{OX}(V_G - V_{th})/q$ for devices II, III, and IV, where V_{th} is the threshold voltage estimated from the measured I-V_G transfer curves, C_{OX} and q are the gate dielectric capacitance and the elementary charge, respectively.[40] For T > 160 K, n of devices

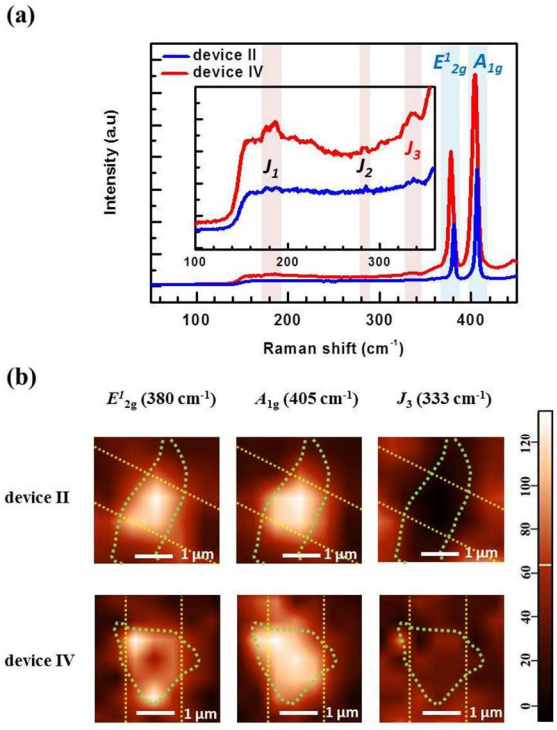

Figure 4. **(a)** Raman spectra obtained from devices II and IV. The inset shows the enlarged Raman spectra in the range from 100 to 360 cm^{-1}. **(b)** Raman mapping images of the E^1_{2g}(380 cm^{-1}), A_{1g}(406 cm^{-1}), and J_3(333 cm^{-1}) obtained from devices II and IV.

II, III, and IV decreased similarly with lowering temperature. For T < 160 K, however, *n* of device IV decreased more slowly than *n* of device II, suggesting that device IV was more doped than device II or III.

MoS_2 is known to have two phases: semiconducting 2H and metallic 1T.[5-8] Mechanically exfoliated MoS_2 flakes usually exhibit the 2H phase because this phase is thermodynamically more stable than the 1T phase.[1-4] However, we conjecture that the metallic 1T phase may also be present in multilayer MoS_2, even though the volume of the 1T phase may be small and may vary from device to device. If there is no 1T phase, the MIC is not expected, as it is for device II. However, if the volume of the 1T phase is finite, the MIC may be observed, as with device VI.

To test our idea, we measured Raman spectra using 532 nm laser line for devices II and IV (Figure 4(a)). The 1T and 2H phases exhibit different Raman spectra, enabling discrimination between these 1T and 2H phases.[9,31-32] For devices II and IV, two typical Raman active modes were observed: the in-plane E^1_{2g} at ~380 cm^{-1} and the out-of-plane A_{1g} at 405 cm^{-1}. However, the peak widths of device II were narrower than those of device IV, implying that the crystal quality of device II might be better than that of device IV. Also, device IV exhibited additional features at ~180 and 333 cm^{-1} that were not found in device II. The 1T-MoS_2 was reported to show Raman peaks at 156 (J_1), 226 (J_2), and 333 (J_3) cm^{-1} that are not normally seen in the Raman spectrum of 2H-MoS_2.[31] Thus, the peak at 333 cm^{-1} might be attributed to the 1T phase in device IV, although J_1 and J_2 were not clearly observed.

Figure 4(b) illustrates the Raman mapping images of the E^1_{2g}, A_{1g}, and J_3 (333 cm^{-1}) modes obtained from devices II and IV, respectively. The intensities of the E^1_{2g} and A_{1g} modes were spatially uniform across device II, whereas the intensity of the J_3 mode (which probably comes from the 1T phase) was negligible, indicating that there was almost no 1T phase in device II. For device IV, however, the intensity of A_{1g} was spatially uniform across the device, but that of E^1_{2g} was not uniformly distributed. Moreover, finite signals of the J_3 mode were detected, suggesting the co-existence of the 1T and 2H phases in device IV. These results support our idea that the metallic 1T phase may be present even in multilayer MoS_2 although the 1T phase volume may vary from device to device, and this 1T phase may cause the MIC in multilayer MoS_2.

One of the characteristics that distinguish semiconductors from metals is the photocurrent effect. The photocurrent of semiconductors is enhanced when exposed to light, whereas that of metals is unchanged. To investigate the photosensitivity of devices II and IV, we measured the real-time photocurrent at room temperature and at different values of V_G. During the measurement, a near-infrared (NIR) laser diode (λ≈808 nm) with a power of 5.3 mW/mm^2 was turned on and off repeatedly (Figure 5). For both devices II and IV, the photosensitivity decreased with increasing V_G, as reported for typical phototransistors.[41-43] However, when light was off, the photocurrent of device II (red line) recovered to the initial value (I_0) immediately, while the photocurrent of device IV (black line) returned to a value higher than I_0 at V_G=-20 V or a value lower than I_0 at V_G=-10, 0, and +10 V. Compared to device II, device IV yielded a much lower photosensitivity at all values of V_G. In particular, the photocurrent of device IV did not nearly increase at V_G=+10 V upon NIR irradiation. This meant that device IV might act as a metal at V_G=+10 V, as observed in the *I*-V_G transfer curves (Figure 2(e)). These results confirmed that the volume of the metallic 1T phase was larger in device IV than in device II.

In summary, we investigated the temperature dependence of the electrical transport properties for more than 20 multilayer MoS_2 FET devices. These devices were classified as having one of three representative characteristics. The first type showed typical n-type semiconducting behaviors, whereas the second or third type exhibited the MIC from metallic to insulating conduction at high positive V_G or $V_G \approx 0$ V. To observe the MIC, good contact between the metal electrodes and MoS_2 was required. To explore the origin of the MIC in multilayer MoS_2, we measured the Raman spectra. In addition to the two typical active Raman modes, E^1_{2g} and A_{1g}, we observed additional Raman features for the devices with the MIC, which might be ascribed to the metallic 1T phases. In contrast, additional Raman peaks were not found for the devices without the MIC. These results suggested that the 1T phase might also exist in multilayer MoS_2, although its volume varied from device to device, and it might be related to inducing the MIC. In addition, compared to devices without the MIC, devices with the MIC yielded a much lower photosensitivity, supporting the presence of the metallic 1T phase.

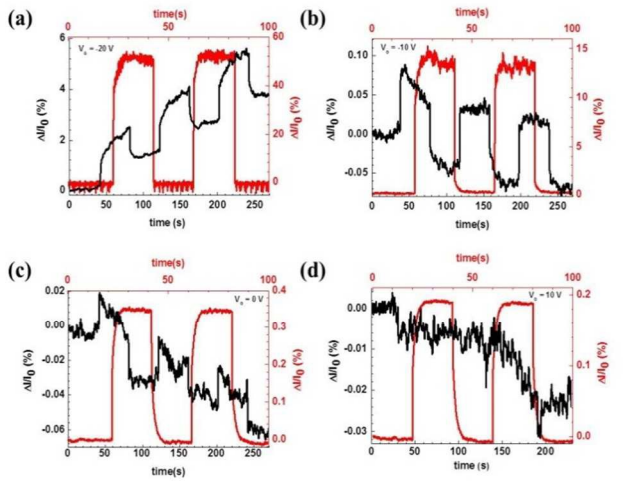

Figure 5. Real-time photoresponse of device II (red line) and device IV (black line) measured while a NIR laser diode (λ ≈ 808 nm) is turned on and off repeatedly at **(a)** V_G = – 20 V, **(b)** V_G = – 10 V, **(c)** V_G = 0 V, **(d)** V_G = 10 V.

Acknowledgements

This work was financially supported by the Basic Science Research Program through the National Research Foundation of Korea (NRF) funded by the Ministry of Science, ICT and Future Planning (Grant No. 2011-0017486 and 2012R1A4A1029061).

Notes and references

[a] Department of Physics, Yonsei University, 134 Shinchon-dong, Seodaemun-gu, Seoul 120-749.KOREA

† Electronic Supplementary Information (ESI) available: [details of any supplementary information available should be included here]. See DOI: 10.1039/c000000x/

1 Y. C. Lin, D. O. Dumcenco, Y. S. Huang and K. Suenaga, *Nat. Nanotechnol.*, 2014, **9**, 391-396.
2 W. Zhou, *Nat. Nanotechnol.*, 2014, **9**, 333-334.
3 Q. H. Wang, K. Kalantar-Zadeh, A. Kis, J. N. Coleman and M. S. Strano, *Nat. Nanotechnol.*, 2012, **7**, 699-712.

4 W. Zhao, R. M. Ribeiro, M. Toh, A. Carvalho, C. Kloc, A. H. Castro Neto and G. Eda, *Nano Lett.*, 2013, **13**, 5627-5634.
5 L. F. Mattheiss, *Phys. Rev. B*, 1973, **8**, 3719-3740.
6 F. Wypych and R. Schollhorn, *J. Chem. Soc., Chem. Commun.*, 1992, 1386-1388.
7 R. Bissessur, M. G. Kanatzidis, J. L. Schindler and C. R. Kannewurf, *J. Chem. Soc., Chem. Commun.*, 1993, 1582-1585.
8 D. Voiry, A. Goswami, R. Kappera, C. e Silva Cde, D. Kaplan, T. Fujita, M. Chen, T. Asefa and M. Chhowalla, *Nat. Chem.*, 2015, **7**, 45-49.
9 R. Kappera, D. Voiry, S. E. Yalcin, B. Branch, G. Gupta, A. D. Mohite and M. Chhowalla, *Nat. Mater*, 2014, **13**, 1128-1134.
10 S. S. Chou, Y. K. Huang, J. Kim, B. Kaehr, B. M. Foley, P. Lu, C. Dykstra, P. E. Hopkins, C. J. Brinker, J. Huang and V. P. Dravid, *J. Am. Chem. Soc.*, 2015, **137**, 1742-1745.
11 R. Kappera, D. Voiry, S. E. Yalcin, W. Jen, M. Acerce, S. Torrel, B. Branch, S. D. Lei, W. B. Chen, S. Najmaei, J. Lou, P. M. Ajayan, G. Gupta, A. D. Mohite and M. Chhowalla, *APL Mater.*, 2014, **2**.
12 B. Radisavljevic, A. Radenovic, J. Brivio, V. Giacometti and A. Kis, *Nat. Nanotechnol.*, 2011, **6**, 147-150.
13 Y. Yoon, K. Ganapathi and S. Salahuddin, *Nano Lett.*, 2011, **11**, 3768-3773.
14 B. Radisavljevic, M. B. Whitwick and A. Kis, *ACS Nano*, 2011, **5**, 9934-9938.
15 S. Das, H. Y. Chen, A. V. Penumatcha and J. Appenzeller, *Nano Lett.*, 2013, **13**, 100-105.
16 K. F. Mak, C. Lee, J. Hone, J. Shan and T. F. Heinz, *Phys. Rev. Lett.*, 2010, **105**.
17 A. Kuc, N. Zibouche and T. Heine, *Phys. Rev. B*, 2011, **83**.
18 A. Splendiani, L. Sun, Y. B. Zhang, T. S. Li, J. Kim, C. Y. Chim, G. Galli and F. Wang, *Nano Lett.*, 2010, **10**, 1271-1275.
19 G. Eda, H. Yamaguchi, D. Voiry, T. Fujita, M. W. Chen and M. Chhowalla, *Nano Lett*, 2011, **11**, 5111-5116.
20 W. Choi, M. Y. Cho, A. Konar, J. H. Lee, G. B. Cha, S. C. Hong, S. Kim, J. Kim, D. Jena, J. Joo and S. Kim, *Adv. Mater.*, 2012, **24**, 5832-5836.
21 H. S. Lee, S. W. Min, Y. G. Chang, M. K. Park, T. Nam, H. Kim, J. H. Kim, S. Ryu and S. Im, *Nano Lett.*, 2012, **12**, 3695-3700.
22 D. Lembke and A. Kis, *ACS Nano*, 2013, **7**, 3730-3730.
23 S. Bertolazzi, J. Brivio and A. Kis, *ACS Nano*, 2011, **5**, 9703-9709.
24 K. K. Kam and B. A. Parkinson, *J. Phys. Chem-US.*, 1982, **86**, 463-467.
25 S. Lebegue and O. Eriksson, *Phys. Rev. B*, 2009, **79**.
26 B. Radisavljevic and A. Kis, *Nat. Mater.*, 2013, **12**, 815-820.
27 B. W. H. Baugher, H. O. H. Churchill, Y. F. Yang and P. Jarillo-Herrero, *Nano Lett.*, 2013, **13**, 4212-4216.
28 K. Kaasbjerg, K. S. Thygesen and K. W. Jacobsen, *Phys. Rev. B*, 2012, **85**.
29 S. V. Kravchenko and M. P. Sarachik, *Int. J. Mod. Phys. B*, 2010, **24**, 1640-1663.
30 H. Qiu, T. Xu, Z. L. Wang, W. Ren, H. Y. Nan, Z. H. Ni, Q. Chen, S. J. Yuan, F. Miao, F. Q. Song, G. Long, Y. Shi, L. T. Sun, J. L. Wang and X. R. Wang, *Nat. Commun.*, 2013, **4**.
31 S. J. Sandoval, D. Yang, R. F. Frindt and J. C. Irwin, *Phys. Rev. B*, 1991, **44**, 3955-3962.
32 J. H. Fan, P. Gao, A. M. Zhang, B. R. Zhu, H. L. Zeng, X. D. Cui, R. He and Q. M. Zhang, *J. Appl. Phys.*, 2014, **115**.
33 J. R. Chen, P. M. Odenthal, A. G. Swartz, G. C. Floyd, H. Wen, K. Y. Luo and R. K. Kawakami, *Nano Lett.*, 2013, **13**, 3106-3110.
34 A. Anwar, B. Nabet, J. Culp and F. Castro, *J. Appl. Phys.*, 1999, **85**, 2663-2666.
35 Y. Zhou, W. Han, Y. Wang, F. X. Xiu, J. Zou, R. K. Kawakami and K. L. Wang, *Appl. Phys. Lett.*, 2010, **96**.
36 E. Abrahams, P. W. Anderson, D. C. Licciardello and T. V. Ramakrishnan, *Phys. Rev. Lett.*, 1979, **42**, 673-676.
37 A. Koga, N. Kawakami, R. Peters and T. Pruschke, *Phys. Rev. B*, 2008, **77**.
38 A. Anwar, B. Nabet, J. Culp and F. Castro, *J. Appl. Phys.*, 1999, **85**, 2663-2666.
39 S. Ghatak, A. N. Pal and A. Ghosh, *ACS Nano*, 2011, **5**, 7707-7712.
40 D. K. Schroder, *Semiconductor material and device characterization*, Wiley, New York, 2006.
41 Z. Y. Yin, H. Li, H. Li, L. Jiang, Y. M. Shi, Y. H. Sun, G. Lu, Q. Zhang, X. D. Chen and H. Zhang, *ACS Nano*, 2012, **6**, 74-80.
42 O. Lopez-Sanchez, D. Lembke, M. Kayci, A. Radenovic and A. Kis, *Nat. Nanotechnol.*, 2013, **8**, 497-501.
43 C. C. Wu, D. Jariwala, V. K. Sangwan, T. J. Marks, M. C. Hersam and L. J. Lauhon, *J. Phys. Chem. Lett.*, 2013, **4**, 2508-2513.